Periodic X-ray Sources in the Galactic Bulge: Application of the Gregory-Loredo Algorithm

Tong Bao,[1,2]⋆ Zhiyuan Li,[1,2]†

[1]*School of Astronomy and Space Science, Nanjing University, Nanjing 210046, China*
[2]*Key Laboratory of Modern Astronomy and Astrophysics (Nanjing University), Ministry of Education, Nanjing 210046, China*

ABSTRACT

We present the discovery of 23 X-ray periodic sources in the Limiting Window (LW), a low-extinction region in the Galactic bulge, locating 80' south of the Galactic center. Their luminosities range($10^{31} - 10^{33}$ erg s^{-1}) and period distribution(mostly between 1 to 3 hour), indicate they are cataclysmic variables (CVs). Most of them are polars with relatively harder spectrum, suggesting an unusual sub-class of mCVs. The brighter sources (6 out of 23 with L>10^{32} erg s^{-1}) in this sample are more likely IPs, with mean M_{WD} about 0.8 $M_\odot$. We also proved that the Gregory-Loredo (GL) method used in this work has better sensitivity and data usage compared to the Lomb-Scargle (LS) method. In combination with the simulation and the geometry of accretion in CVs, we constrain the proportion of polars to X-ray sources in LW about 16%, and the fraction of DNe is about 45%, though with more uncertainty. Still, this discovery confirms the sub-type of unusual mCVs and provides a practical way to study the population about X-ray sources based on periodic modulation.

Key words: Galaxy: bulge — X-rays: stars — X-rays: binaries

1 INTRODUCTION

Cataclysmic variables (CVs) are close binary including a white dwarf (WD) and a main-sequence or sub-giant companion, whose material could be accreted by Roche-lobe overflow or stellar wind. They can be divided into magnetic (mCVs) and nonmagnetic CVs (non-mCVs) according to their magnetic field strengths of WDs. In addition, the mCVs are split into polars ($P_{spin}/P_{orb} \simeq 1$) and IPs ($P_{spin}/P_{orb} \simeq 0.01 - 1$), depending on their level of synchronization. The evolution of CVs are driven by angular momentum losses (AML) to keep the period from expanding, which would made system detached. The existence of "period gap" is caused by the change of mechanism for angular momentum losses. The dominant AML mechanism in long-period systems ($P_{orb} \geq 3$ hour) is "magnetic braking", whereas short-period CVs ($P_{orb} \leq 2$ hour) are driven by gravitational radiation. Meanwhile, there is a minimum period of CVs, resulted from the mass-loss-induced loss of thermal equilibrium in companion star. The orbital period of CVs are mainly between 1 to 10 hours, making it suitable for X-ray timing analysis.

It has been proved that the collective properties of CVs serve as great probe for dynamic interactions of their local environment, contributed from the high abundance of WDs in binaries. The effect would be remarkable only with extremely high stellar density (e.g. galactic center or global clusters (Cheng et al. 2019)) for us obtaining observable evidence in Hubble time. In addition to that, the individual properties of CVs provide hints for the accretion region and magnetic field, especially from their periodic variability.

It has been suggested that the thousands of X-ray sources in galactic center are magnetic cataclysmic variables, particularly intermediate polars (IPs) (Muno et al. 2009; Zhu et al. 2018). Due to the lack of optical/infrared imaging and spectroscopy resulted from high extinction and source crowding, the direct identification of them has been really difficult. In fact, even the presence and characteristics of the He II λ4686 and Hβ line have been often used to judge if a CV is magnetic or not, the proof is far from conclusive. In Silber (1992), many IPs with weak Hβ lines could not be identified from non-magnetic systems using this diagnostic. Hence the periodicity becomes a well recognized probe to study their population, because of their different features in periodic modulation (see Section 6.2).

In Muno et al. (2003), eight periodic sources were identified as mCVs in galactic center region (GCR). Then for galactic bulge region, ten periodic sources were found by using Lomb-Scargle methods (Hong et al. 2012). They were believed as an unusual type of mCVs with harder spectra like IPs while their period distribution resembles that of polars. The research was based on the observation of low-extinction Window fields (LW), locating at 1°4 south of the Galactic center. Its rarity of avoiding the obscuration from molecular cloud deserved our deeper excavation of these X-ray sources. Besides, according to RK catalog (Ritter & Kolb 2003), the mCVs (mostly DNe) occupied 20% in CVs sample, while for GCR, this fraction was reckoned over 30-40% (Hailey et al. 2016; Hong et al. 2012). The miss of non-mCVs demands reliable explanation from

Table 1. *Chandra* observations of the Limiting Window

ObsID	Start Time UT	Nominal R.A. (○)	Nominal Decl. (○)	Roll angle (○)	Exposure ks	Mode
6362	2005-08-19 16:15	267.86875	-29.58800	273	37.7	FAINT
5934	2005-08-22 08:16	267.86875	-29.58800	273	40.5	FAINT
6365	2005-10-25 14:55	267.86875	-29.58800	265	20.7	FAINT
9505	2008-05-07 15:29	267.86375	-29.58475	82	10.7	VFAINT
9855	2008-05-08 05:00	267.86375	-29.58475	82	55.9	VFAINT
9502	2008-07-17 15:45	267.86375	-29.58475	281	164.1	VFAINT
9500	2008-07-20 08:11	267.86375	-29.58475	280	162.6	VFAINT
9501	2008-07-23 08:13	267.86375	-29.58475	279	131.0	VFAINT
9854	2008-07-27 05:53	267.86375	-29.58475	278	22.8	VFAINT
9503	2008-07-28 17:37	267.86375	-29.58475	275	102.3	VFAINT
9892	2008-07-31 08:07	267.86375	-29.58475	275	65.8	VFAINT
9893	2008-08-01 02:44	267.86375	-29.58475	275	42.2	VFAINT
9504	2008-08-02 21:23	267.86375	-29.58475	275	125.4	VFAINT

analyzing the properties of these sources. It may indicates that a large number of non-mCVs still awaits discovery since faint class can be always missed in flux-limited surveys.

In this work, we have taken full usage of *Chandra* observations for LW. Meanwhile, the methods with more efficiency and the simulation with higher accuracy have been both operated. We explored the X-ray properties of 23 periodic sources (ten of them identified in Hong et al. (2012)). Section 2 describes the observation we used and the source detection process. Section 3 gives a brief overview about the main methods for period finding and focuses on the GL method we adopted in this work. Section 4 is devoted to the confirmation of period finding results. Section 5 presents the spectra analysis for these periodic sources and the estimation of mass of WDs based on the Fe line diagnostic. The comparison with previous work , the identification for these periodic sources and the X-ray source population in the LW would be discussed in Section 6.

2   X-RAY DATA PREPARATION

2.1   *Chandra* observations

The LW towards the inner Galactic bulge has been extensively observed by *Chandra* with its Advanced CCD Imaging Spectrometer (ACIS). A total of 13 ACIS-I observations were taken, three in 2005 and ten in 2008, resulting in a total exposure of 982 ks. A log of these observations is given in Table 1. A number of previous studies have made use of all or part of these observations, which primarily focused on the identification of discrete X-ray sources and the quantification of their statistical properties (Revnivtsev et al. 2009; van den Berg et al. 2009; Hong et al. 2009; Revnivtsev et al. 2011; Hong 2012; Morihana et al. 2013; Wevers et al. 2016).

We downloaded and uniformly reprocessed the archival data with CIAO v4.10 and CALDB v4.8.1, following the standard procedure[1]. The CIAO tool *reproject_aspect* was employed to align the relative astrometry among the individual observations, by matching the centroids of commonly detected point sources. ObsID 9502, which has the longest exposure (164.1 ks), served as the reference frame. The level 2 event file was created for each ObsID, with the arrival time of each event corrected to the Solar System barycenter (i.e., Temps Dynamique Barycentrique time) by using the CIAO

tool *axbary*. We then constructed a merged event list, reprojecting all events to a common tangential point, [R.A., Decl.]=[267.86375, 29.58475]. The individual observations cover a similar field-of-view (FoV) due to their similar aimpoints and roll angles, as illustrated in Figure 1 which displays the merged 2–8 keV counts image. We have examined the light curve of each ObsID and found that the instrumental background was quiescent for the vast majority of time intervals. Hence we preserved all the science exposures for source detection and subsequent timing analysis, taking the advantage of uninterrupted signals within each observation.

2.2   Source detection

It is known that the LW suffers from moderate line-of-sight extinction, $N_{\rm H} \approx 7 \times 10^{21}$ cm^{-2} (Revnivtsev et al. 2011), which obscures X-ray photons with energies $\lesssim 1$ keV. Here we focus on sources prominent in the 2–8 keV band, which are most likely CVs located in the Galactic bulge. This will also facilitate a direct comparison with the CVs found in the Nuclear Star Cluster (Zhu et al. 2018), the line-of-sight column density of which, $N_{\rm H} \sim 10^{23}$ cm^{-2}, is only transparent to photons with energies $\gtrsim 2$ keV.

Source detection was performed following the procedures detailed in Zhu et al. (2018). Briefly, we first generated for each observation an exposure map as well as point-spread function (PSF) maps with enclosed count fraction (ECF) of 50% and 90%. Both the exposure and PSF maps were weighted by a fiducial spectrum, which is an absorbed bremsstrahlung with a plasma temperature of 10 keV and a column density of $N_{\rm H} = 10^{22}$ cm^{-2}, representative of the X-ray sources in the LW. We then reprojected the individual exposure maps to form a stacked exposure map in the same way as for the counts images; the PSF maps were similarly stacked, weighted by the corresponding exposure map. Next, we employed *wavdetect* to identify discrete sources in the merged 2–8 keV counts image, supplying the algorithm with the stacked exposure map and the 50%-ECF PSF map and adopting a false-positive probability threshold of 10^{-6}. This resulted in a raw list of 847 independent sources in the 2–8 keV band.

The source centroid derived from *wavdetect* was refined using a maximum likelihood method that iterates over the detected counts within the 90% enclosed counts radius (ECR). Starting from this step we consider the 1–8 keV band to maximize the signal from potential sources in the LW. Then, for each ObsID, source counts were extracted from the 90% ECR, while background counts were

[1] http://cxc.harvard.edu/ciao
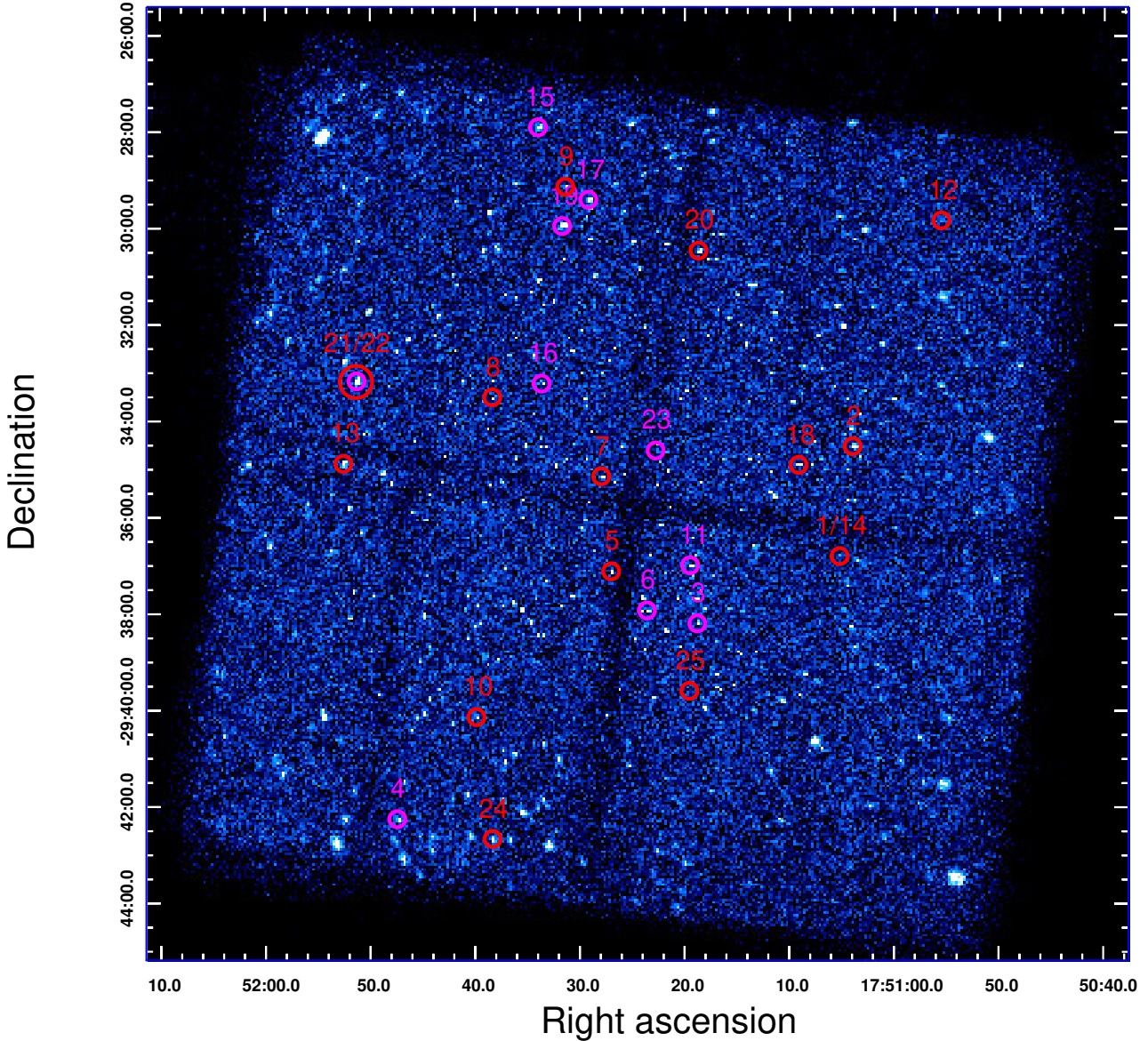
Figure 1. 2–8 keV counts image of the Limiting Window, combining 13 *Chandra*/ACIS-I observations. Locations of the 23 periodic sources are marked with colored circles (*magenta*: ten sources previously reported by (Hong et al. 2012); *red*: thirteen newly discovered in this work). Source numbering is the same as in Table 2. In particular, 1/14 and 21/22 are the two sources each showing two periodic signals.

extracted from a concentric annulus with inner-to-outer radii of 2–4 times the 90% ECR, excluding any pixel falling within 2 times the 90% ECR of neighboring sources. Source crowding is not a general concern in the LW, but in a few cases the source extraction region was reduced to 50% ECR due to otherwise overlapping sources. The total source and background counts were obtained by summing up the individual observations. Photometry (i.e., net photon flux and its error) for individual sources were calculated using the CIAO tool *aprates*, which takes into account the local effective exposure, background and ECF. We consider a *significant detection* for a given source in a given ObsID if the photon flux is greater than 3 times the error. We further define for each source an inter-observation *variability index*, VI = S_{max}/S_{min}, where S_{max} and S_{min} are the maximum and minimum photon fluxes among all the significant detections, respectively. This implicitly requires significant detections in at least two observations.

3 PERIOD SEARCHING METHOD

In this section, we first provide our motivation of employing the Gregory-Loredo (GL) algorithm, followed by an outline of its basic principles (Section 3.1). We then describe our application of the GL algorithm to the *Chandra* data of the LW (Section 3.2). This is complemented by a set of simulations to evaluate the detection (in)completeness of periodic signals (Section 3.3).

3.1 The Gregory-Loredo Algorithm

There exists in the literature a variety of period searching methods, which can be broadly divided into three categories according to their working principles.

The most traditional method is based on Fourier transform and its power density spectra, which includes the classical Schuster

periodogram (Schuster 1898), the Fourier analysis with unequally-spaced data (Deeming 1975), the correlation-based method (Edelson & Krolik 1988), among others.

Another widely-used method seeks to fit the data with a periodic model in the frequency space, employing statistics such as least-squares residuals to define the likelihood function and then selecting the frequency that maximizes the likelihood. The famous Lomb-Scargle periodogram (Lomb 1976; Scargle 1982, hereafter LS) belongs to this category. Note that when adopting trigonometric functions, the least-squares method falls into the Fourier transformation category. Another variant is to replace the least-squares residuals with polynomial fits, such as that used in Schwarzenberg-Czerny (1996).

The last category is the phase-folding method. For each trial period the time-tagged data is folded as a function of phase, and the best-fit period is found by optimizing the cost function through the frequency space. The cost function is designed to evaluate how much the phase-folded light curve deviates from constant. Methods belonging to this category use diverse cost functions. Several widely known examples are the Epoch Folding (EF) algorithm (Leahy et al. 1983), the Phase Dispersion Minimization (Stellingwerf 1978), and the GL algorithm (Gregory & Loredo 1992).

In X-ray observations, the detection of periodic signals is often involved with irregularly and sparsely sampled data. When working in frequency space, such a sampling can lead to spurious signals and hevay contamination to the real signal. Phase-folding methods, on the other hand, can avoid the effect of non-uniform data since the dead time does not enter the algorithm. Moreover, the number of detected source counts is often only moderate. While one can in principle apply binning to create photometric light curve, it takes the price of potentially losing temporal information. Phase-folding methods, on the other hand, directly handle individual events, thus maximally incorporating the temporal information.

Most X-ray sources in the LW share the characteristics of irregular sampling and limited source counts. Therefore, it is appropriate to employ the GL algorithm, which applies the Bayesian probability theory to the phase-folded light curve, to search for periodic signals for the LW sources. We provide a brief overview of Bayes's theorem and the GL algorithm in Appendix A. The key of this algorithm is the multiplicity of the phase distribution of events,

$$W_m(\omega, \phi) = \frac{N!}{n_1! \, n_2! \, n_3! \cdots n_m!}. \qquad (1)$$

Here N represents the total number of counts of a given source, $n_i(\omega, \phi)$ is the number of events falling into the ith of m phase bins given the frequency ω and the phase ϕ, satisfying $\sum_{i=1}^{m} n_i(\omega, \phi) = N$. The multiplicity is the number of ways that the binned distribution could have arisen by chance. It can be easily shown that the more the values of n_i differ from each other, the smaller the multiplicity. In other words, the more the piecewise model defined the m phase bins deviates from constant, the more likely there exists a periodic signal, the probability of which is inversely proportional to the multiplicity.

In general, the GL algorithm takes the following steps:

(i) Compute the multiplicity for all sets of (m, ω, ϕ) (Eqn. 1). In this work, the highest value of m is set to be 12.

(ii) Given m, integrate over the (ω, ϕ) space and calculate the so-called "odds ratio" using Bayes's theorem (Eqn. A16). The "odds ratio" determines the ratio of probabilities between a periodic model and a non-periodic (constant) model.

(iii) Sum up the normalized odds ratios of each m to determine the probability of a periodic signal (Eqn. A20). If this probability exceeds a predefined threshold (for instance, 90%), a periodic signal is favored.

(iv) Finally, compare all the odds ratios integrated over the ϕ space, finding the value of ω with the highest odds ratio, which then gives the period $P = 2\pi/\omega$ (Eqn. A21).

3.2 Application to the LW

We apply the GL algorithm to search for periodic signals in the LW sources. For a given source, the 1–8 keV counts within the 90% ECR of individual ACIS-I observations are extracted to form a time series. In addition, we supply for each source the information of "epoch", i.e., the start time and end time of each ObsID in which the source has at least one detected count. This information is used to compensate for the uneven distribution over the phase bins (see Eqn. A17 for a detailed illustration). Since the GL algorithm determines the probability of a periodic signal against a constant light curve, there is no need to separately account for the background level, which is absorbed into the constant. Nevertheless, we have measured the local background (Section 2.2) for each periodic source as a consistency check (see Section 4).

As mentioned in Section 3.1, the GL algorithm folds the time series at a trial frequency (or period). In practice, the resolution and range of frequency must be compromised between accuracy and computational power. Thus we restrict our analysis on three period ranges: (300, 3000), (3000, 10000) and (10000, 50000) sec, with a frequency resolution of 10^{-7}, 10^{-8} and 10^{-9} Hz, respectively. The period ranges are chosen based on the expectation that most, if not all, detectable periodic X-ray sources in the LW should be CVs. The orbital period distribution of CVs is known to exhibit a minimum at about 70 minutes, a gap between 2–3 hours, and a maximum around 10 hours (Ritter & Kolb 2003). The second and third period ranges well cover these characteristic periods, whereas the first range probes the spin period of fast rotating IPs. Given the timespan of $\sim 10^8$ sec between the first and last ACIS-I observations, the chosen frequency resolutions are optimal for an efficient search of periodic signals.

3.3 Detection completeness

For a given period searching algorithm, the detection rate depends on both the number of observed counts, the intrinsic shape of the light curve, as well as the observing cadence. To quantify the detection rate and hence gain insight on the nature of the periodic sources in the LW, we perform simulations following the merit of Cicuttin et al. (1998). Two functional forms of light curve are considered: a sinusoidal function and a piecewise function. While these are admittedly idealized shapes, they can represent realistic light curves, e.g., the former resulted from rotational modulation and the latter due to eclipse.

A sinusoidal light curve follows,

$$\lambda(t) = \lambda_0[1 + A_0 \sin(\omega t + \phi)], \qquad (2)$$

where $\omega = 2\pi/P$, A_0 is the relative amplitude of variation, and λ_0 is the mean count rate which may include contribution from a constant background. The phase ϕ can be arbitrarily set at zero. For a direct comparison with observations, we relate λ_0 with the total number of counts, $C = \lambda_0 T$, where T is the exposure time of a given observation. This holds since T is typically much longer than the modulation period (P). The simulations are run with a selected number of parameters due to constraints in computational

power. Specifically, we adopt C=50, 100, 200, 300, 400 and 500, A_0=0.5, 0.6, 0.7, 0.8 and 0.9, and P=554, 5540 and 45540 sec, resulting in a total of 6x5x3=90 combinations. The chosen periods are representative of the actually searched ranges (Section 3.2), whereas the adopted total counts well sample the range of observed counts from the LW sources.

We thus simulate 100 light curves for each combination of parameters, taking into account Poisson errors and the exact start and end times of the 13 ACIS-I observations. The arrival time of each simulated count is further randomly modified by an amount of 3.2 sec to mimic the effect of ACIS frame time. The simulated light curve is then searched for a periodic signal using the GL algorithm in the same manner as for the real data (Section 3.2). We count a valid detection if the found period has a detection probability greater than 90% and its value consistent with the input period to within 1%. We notice that in a small fraction of simulated light curves of the shortest input period (554 sec), the second harmonics (i.e., 2 times the true period) is detected with an even higher probability than the true period. We also consider such cases a valid detection as long as the true period itself fulfills the above criteria.

The detection rate for a given combination of parameters is taken to be the fraction of the 100 simulated light curves having a valid detection. The top, middle and bottom panels of Figure 2 show the result of the three test periods, respectively, in which several trends are apparent. First and intuitively, for a given period and amplitude, higher total counts would lead to higher detection rates, while for given total counts, a higher amplitude also leads to a higher detection rate. The simulation results confirm these expectations. Second, for the same total counts and amplitude, the detection rate is generally higher for a longer period. This can be understood as due to a statistical behavior in the multiplicity (see Eqn. 1), which has a lower value for a long period. This holds for both the sinusoidal and piecewise light curves. Lastly, for total counts of 50, the detection rate is almost always below 10% regardless of the period and amplitude.

The piecewise function, which mimics an eclipse against an otherwise constant flux, takes the form of

$$\lambda(t) = \begin{cases} \lambda_0 & \phi(t) \in [0, (1-w)\pi) \cup ((1+w)\pi, 2\pi], \\ f\lambda_0 & \phi(t) \in [(1-w)\pi, (1+w)\pi], \end{cases} \quad (3)$$

where w accounts for the eclipsing width (duration) in phase space, and f characterizes the relative depth of the eclipse ($0 \le f \le 1$; $f = 0$ corresponds to total eclipse). Here the middle of eclipse is assumed to occur at $\phi = \pi$. Again, λ_0 can be related to the total counts as $C = [1-(1-f)w]\lambda_0 T$. We set $f = 0.1$ and $w = 0.1$ in our simulations, which are not atypical of eclipsing CVs. We test three values of the period, P=5258, 15258 and 45258 sec and adopt trial count rates $\lambda_0 = 1, 2, 3, 4, 5, 6, 7, 8, 9, 10, 15$ and 20×10^{-4} cts s^{-1}. For each combination of parameters, 100 simulated light curves are again generated and fed to the GL algorithm. The resultant detection rate (also taking 90% as the threshold) is shown in Figure 3. As expected, the detection rate is generally higher for a longer period. It can also be seen that for total counts below ∼300, the detection rate is ≲10% regardless of the period; only when total counts exceed ∼1500, the detection rate becomes 100% for all test periods.

We have also run simulations to estimate the rate of false detection, which refers to the detection of a periodic signal from an intrinsically constant light curve. Considering that most LW sources can have a low-amplitude long-term variation, we approximate a semi-constant light curve with a sinusoidal function with P=5 yr and A_0=0.5. Simulated light curves are generated with totals counts
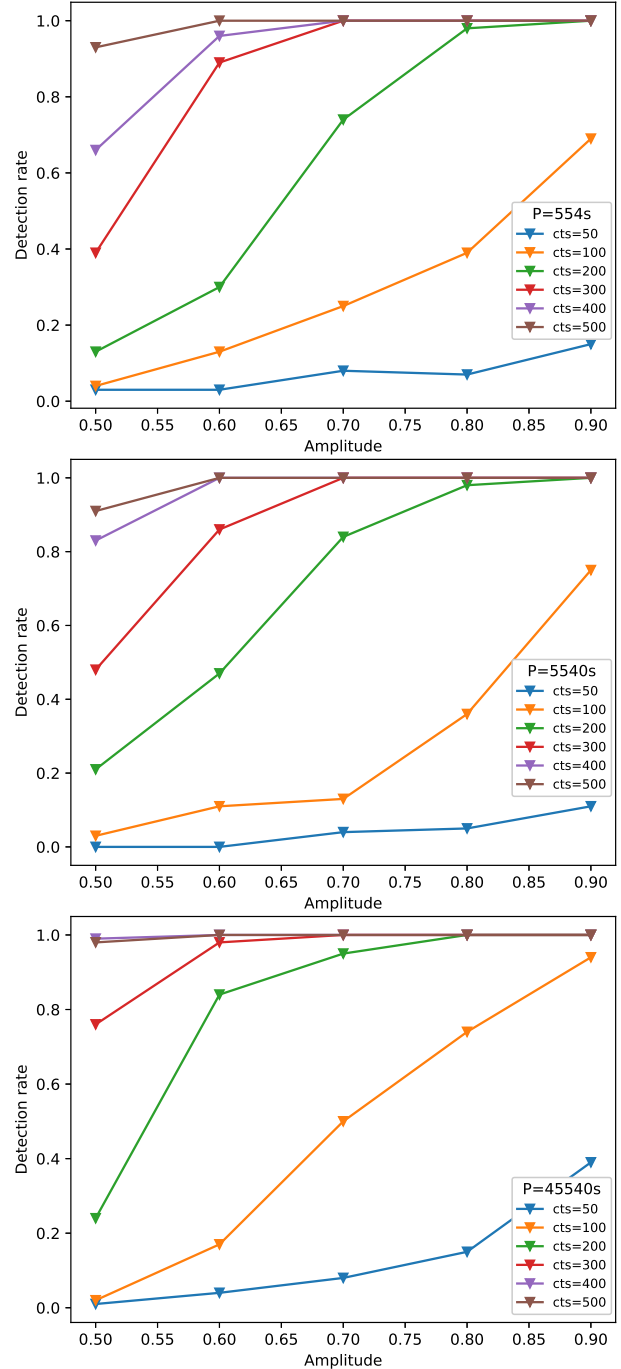
Figure 2. Detection rates as a function of relative variation amplitude, based on simulated sinusoidal light curves. The top, middle and bottom panels are for modulation period of 554, 5540 and 45540 sec, respectively. The different colored lines represent different values of total counts, as labeled. See text for details.

from 50 to 5000 and fed to the GL algorithm. No false detection of periodic signals, at any value between 300–50000 sec, is found. Therefore, it seems safe to conclude that the false detection rate is essentially zero for the GL algorithm applied to the LW data.

Figure 3. Detection rates as a function of total counts, based on simulated piecewise light curves. Different colored lines represent different periods, as labeled. See text for details.

4   PERIOD SEARCHING RESULTS

According to the simulations in Section 3.3, a periodic signal is hard to detect in LW sources with total counts $C < 100$, even in the case of high variation amplitudes. Therefore, we restrict our period searching to sources with $C \geq 100$, which include 667 of the 847 sources in the raw list.

Adopting a probability threshold of 90%, we obtain 48 tentative periodic signals from the three period ranges. However, it is necessary to filter spurious detections, which may be caused by several effects:

(i) By design, the ACIS is dithered to distribute photons over more CCD pixels to avoid pile-up and to fill CCD gaps. The dither period is 706.96 s in pitch and 999.96 s in yaw. Any signal detected at these two periods and their harmonics are thus excluded. These are mostly found in sources located close to CCD gaps, where dithering significantly reduces the number of detected counts in a periodic fashion.

A related concern is how dithering would affect the detection of genuine periods. We run simulations to test this effect. Specifically, we generate simulated sinusoidal light curves with $P = 5072.97$ sec and $C = 293$. This choice is motivated by one particular periodic source (#5 in Table 2), which has a fractional detector coverage of 0.74 (in other words, 26% of the intrinsic flux is lost due to dithering into the CCD gap), the lowest among all valid periodic sources (see below). The dithering effect is mimicked by artificially removing the simulated counts according to a probability distribution calculated by the CIAO tool *dither_region*. No difference is found in the resultant detection rate, compared to that without dithering.

(ii) In certain sources, multiple detections can be caused by second and third harmonics of the same intrinsic signal (i.e., 2 and 3 times the true period). These can be easily identified by the sign of double-peak or triple-peak in the phase-folded light curve, provided that the intrinsic signal has a single-peak structure.

However, the intrinsic structure might be double-peaked, in which case it is more difficult to distinguish between the true period and the half harmonic (i.e., half the true period), in particular when the two peaks have a similar strength and width. Generally speaking, the double-peaked shape only occurs in IPs with an accretion column over each magnetic pole. When viewed from certain angle, the two poles alternatively drift across the front side of the WD, pro-

ducing the double-peaked X-ray light curve. The modulation period in this case must be the spin period of the WD, typically under one hour. Among our tentative detections, most of those showing a double-peaked light curve have a corresponding period longer than 3 hours, far beyond the range of spin periods in IPs. These are probably second harmonics rather than a genuine spin period. Hence we assume that there is no half harmonics in the LW sources and always take the lowest period as the true period. This assumption is supported by our extensive simulations presented in Section 3.3, in which no half harmonic (the true period is known before hand) is found.

(iii) Strong flux variations or outbursts occupying one particular observation can also cause a false periodic signature. This is because the GL algorithm, which analyzes the phase-folded light curve, can be fooled if there were too many photons found in a single observation, producing excess in certain phase bins. In this case the algorithm may "think" there exists a period especially in the period range of (10000, 50000) sec. Among the sources with tentative periods, four exhibit a variability index VI> 10, indicating strong variations. We thus reanalyze their light curves using two subsets of observations: those covering only the outburst and those excluding the outburst. For three of them, the tentative period cannot be recovered in either subset. Therefore, these three are probably fake signals. The remaining source is retained since its period can be recovered in both the outbursting and quiescent subsets.

The above filtering thus results in 25 valid periodic signals in 23 sources. Among them, 10 signals were previously reported by Hong et al. (2012) and are confirmed here with the GL algorithm, while the remaining 15 periods are new discoveries (a comparison between our work and Hong et al. 2012 is further addressed in Section 6.1). The basic information of these periodic sources are listed in Table 2, sorted by the order of increasing period. The source locations are marked in Figure 1.

Two sources each exhibit two different periods, hence we have assigned each of them two IDs: #1/#14 and #21/#22. The phase-folded light curves at the two modulation periods are shown for source #1/#14 in the upper panels of Figure 4 and for source #21/#22 in the upper panels of Figure 5. The number of phase bins, between 20 to 50, is chosen to optimally display substructures in the light curve. While the GL algorithm does not rely on quantifying the local background, for comparison we plot in these panels the estimated background level (yellow strip, the width of which represents 1σ Poisson error; Section 2.2). We defer discussions on the shape of the light curve, which contains important information on the nature of the periodic sources, to Section 6.2.

The phase-folded light curves are complemented by the long-term, inter-observation light curve, shown in the lower left panel of Figures 4 and 5, and by the source spectrum (see Section 5), shown in the lower right panel of Figures 4 and 5. Similar figures of the remaining 21 sources are presented in Appendix B.

5   X-RAY SPECTRAL ANALYSIS

We perform spectral analysis for all 23 confirmed periodic sources to gain insight on their nature. Source and background spectra are extracted from the same regions as described in Section 2.2, along with the ancillary response files (ARFs) and redistribution matrix files (RMFs), by using the CIAO tool *specextract*. The spectra from individual observations are then coadded to form a combined spectrum of a given source, with the corresponding ARFs and RMFs weighted by the effective exposure. Further, the spectrum is adap-

Table 2. Information on the periodic X-ray sources in the Limiting Window

ID LW	R.A. °	Decl. °	Period (s)	P_{GL}	H-ID	C	P_{det} %	VI	Harmonics
(1)	(2)	(3)	(4)	(5)	(6)	(7)	(8)	(9)	(10)
1†	267.77173	-29.61332	853.83	0.90277	-	202	-	1.92	-
2	267.76657	-29.57529	3820.83	0.99222	-	902	-	1.94	-
3	267.82829	-29.63660	4728.90	1.00000	H6	394	99	2.13	Third
4	267.94766	-29.70427	4886.79	0.99994	H8	784	98	1.90	-
5	267.86255	-29.61859	5072.97	0.99933	-	293	-	2.34	Second
6	267.84831	-29.63212	5130.57	1.00000	H2	437	100	2.51	Second
7	267.86651	-29.58575	5144.97	0.99880	-	335	-	2.48	Second
8	267.90982	-29.55845	5158.75	1.00000	-	121	-	2.30	Second
9	267.88075	-29.48562	5231.49	0.94949	-	347	-	1.65	-
10	267.91616	-29.66900	5252.93	0.91425	-	211	-	-	-
11	267.83116	-29.61651	5261.93	1.00000	H10	438	31	1.46	Second
12	267.73141	-29.49721	5334.76	0.99952	-	760	-	1.25	Second
13	267.96901	-29.58142	5501.16	0.99094	-	512	-	2.89	-
14†	267.77173	-29.61332	5608.21	0.96821	-	202	-	1.92	Third
15	267.89161	-29.46508	6335.85	1.00000	H5	823	100	2.09	Second
16	267.89024	-29.55369	6597.55	1.00000	H9	487	99	4.30	Second
17	267.87162	-29.49011	7448.98	0.99999	H3	535	100	1.76	Second
18	267.78806	-29.58177	7756.19	0.99941	-	214	-	4.76	Second
19	267.88203	-29.49922	8546.28	1.00000	H4	3402	93	3.27	Second
20	267.82785	-29.50770	8844.82	0.90987	-	263	-	1.82	Second
21‡	267.96375	-29.55290	9877.52	0.99992	-	1963	-	1.44	-
22‡	267.96375	-29.55290	10342.30	1.00000	H1	1963	99	1.44	-
23	267.84487	-29.57680	12002.70	1.00000	H7	307	100	1.86	Second
24	267.90974	-29.71112	42219.03	1.00000	-	1039	-	23.6	-
25	267.83142	-29.65992	47317.12	0.98850	-	138	-	-	-

Notes: (1) Source sequence number assigned in the order of increasing period. The same source with multiple period signal was denoted as †and ‡. (2) R.A.(J2000) of the centroid of source. (3) Decl.(J2000) of the centroid of source. (4) The modulation period determined by GL method. (5) The probability of periodic signal defined by Eqn. A20. (6) The cross-match results with previous work. H_i represents the ith source in Table 2 of Hong et al. (2012). (7) The number of counts in the 1-8 keV band. (8) The detection probability of periodicity based on simulations of 100 sinusoidal light curves for each source. (9) The detection probability of periodicity simulated as the same process described in column(9), while the amplitude are taken from Hong et al. (2012). (10) VI = S_{max}/S_{min}, where S_{max} and S_{min} are the maximum and minimum photon fluxes among all the valid detections. For source #10 and #25, no VI are provided since the lack of valid detections. (11) The note gives the significant harmonic detected by the algorithm.

tively binned to achieve a minimum of 20 counts and a signal-to-noise ratio greater than 2 per bin.

The resultant spectra are analyzed using XSPEC v12.9.1. Since these sources are expected to be CVs, we adopt a fiducial spectral model (Zhu et al. 2018; Xu et al. 2019), which consists of a bremsstrahlung continuum and three Gaussian lines centered at 6.40, 6.68 and 6.97 keV, all these components subject to an unknown line-of-sight absorption (*phabs* in XSPEC). The three lines (hereafter referred to as the 6.4, 6.7 and 7.0 keV lines) correspond to neutral Fe Kα, Fe XXV Kα and Fe XXVI Lyα, respectively, which are among the most commonly detected emission lines in CV spectra. The latter two lines, in particular, arise from the post-shock plasma near the WD surface, and their flux ratio ($I_{7.0}/I_{6.7}$) has proven to be a robust tracer of the plasma temperature, hence also a good indicator of the WD mass (Xu et al. 2016).

It turns out that the plasma temperature (T_b) is not well constrained in most sources, due to a moderate number of counts and the insufficient sensitivity of *Chandra* at energies above 8 keV. Hence for such cases we fix T_b at 40 keV, which is typical of IPs when their hard X-ray (up to tens of keV) spectra are available (Xu et al. 2016; Hailey et al. 2016). Setting a lower value of T_b, for instance, at 20 keV, does not affect our following conclusions.

Again due to the limited number of counts, most of the periodic sources show weak or non-detected Fe lines. We have applied a bootstrapping method using the *multifake* tool in XSPEC to derive the 90% confidence range for the fluxes of the three Fe lines. It turns out that only one sources, #21 (same as #22), shows a significant line at both 6.7 keV and 7.0 keV. The flux ratio and its 90% error are similarly determined for this sources, resulting in $I_{7.0}/I_{6.7} = 0.91^{+1.22}_{-0.56}$ for #21. According to the empirical line ratio–WD mass ($I_{7.0}/I_{6.7}$–M_{WD}) relation of Xu et al. (2019), which is calibrated with CVs in the solar neighborhood, we can infer $M_{WD} \approx 0.8\,(1.2)\,M_\odot$ for #21, provided that both sources are IPs (DNe). It is noteworthy that there exists no empirical $I_{7.0}/I_{6.7}$–M_{WD} relation for polars, mainly due to the small number of known polars in the solar neighborhood (Xu et al. 2019).

We further divide the 23 periodic sources into two groups based on their luminosities. The H (L) group consists of 6 (17) sources having an unabsorbed 1–8 keV luminosity above (below) 1.0×10^{32} erg s^{-1}, which is derived from the individual best-fit spectral model. The cumulative spectrum of each group is fitted with the same fiducial model, i.e., bremsstrahlung plus three Gaussian lines. The improved S/N in the cumulative spectrum allows us to detect all three Fe lines and constrain their flux ratios. The group has
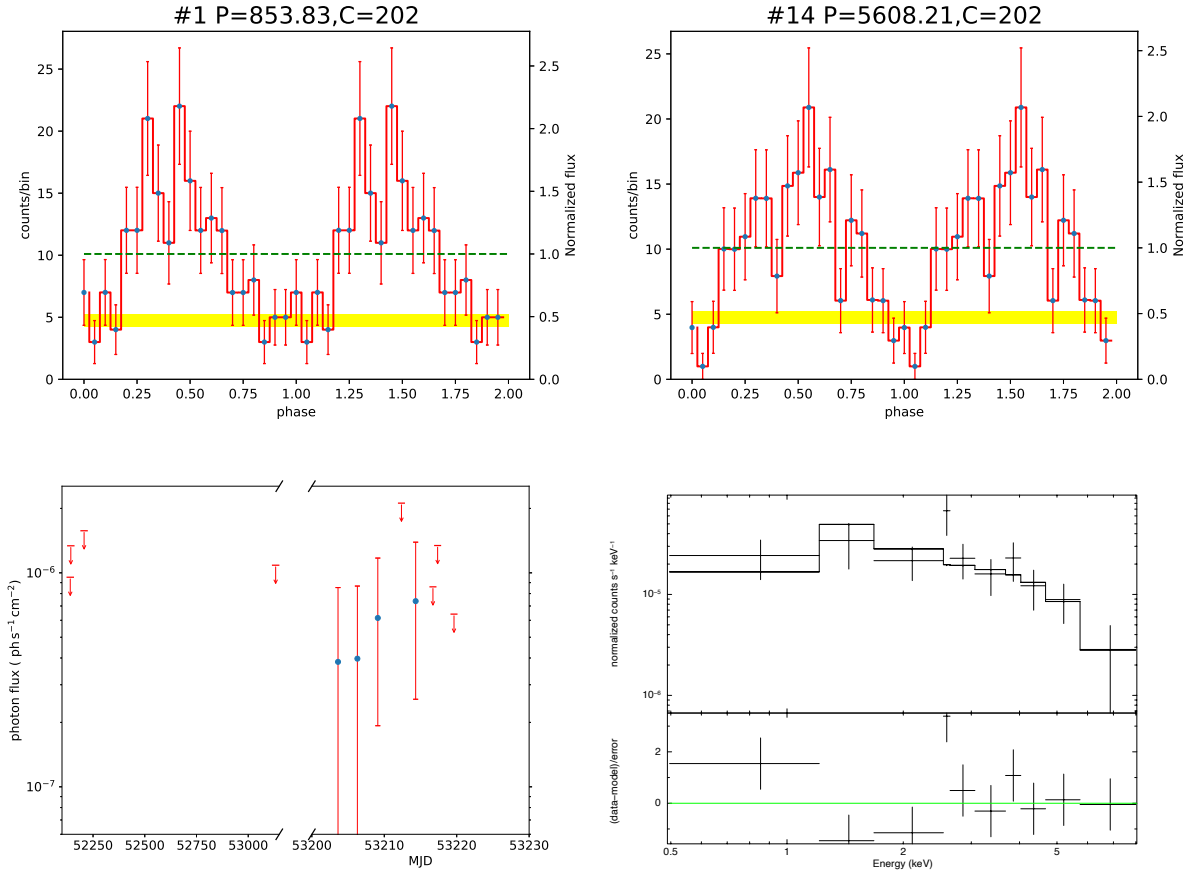
Figure 4. The phase-folded light curve at the two modulation periods (up), the long-term, inter-observation light curve (lower left) and the spectra (lower right) for #1(#14) source. For lower left panel, the valid detection (defined in Section 2.2) are plotted with dots plus error range. While the non-valid detection are shown in arrows, providing only the upper limits. Meanwhile, the x-axis in lower left panel were plotted in discontinuous style for better demonstration effect, since the short interval over the last eight observations. For lower right panel, the spectrum are plotted over 0.5-8 keV.

$I_{7.0}/I_{6.7} = 0.78^{+0.18}_{-0.16}$, thus inferring a mean WD mass of $M_{\rm WD} \approx$ 0.8 (1.2) $M_\odot$ if they are IPs (DNe). On the other hand, the L group shows no constrain of line ratio, we can only provide its upper limit, i.e., 0.39, corresponding $M_{\rm WD} < 0.45$ (0.80) $M_\odot$ if they are IPs (DNe).

Results of the above spectral analysis are summarized in Table 3.

6   DISCUSSION

In this section, we discuss the most significant implications of our results. We first provide a comparison between our work and Hong et al. (2012) (Section 6.1). Then, we try to classify the periodic sources based on their temporal and spectral properties, demonstrating that the majority of these sources are most likely magnetic CVs (Section 6.2). Lastly, we assess the potential sub-populations of CVs in the Galactic bulge (Section 6.3).

6.1   Comparison with previous work

We have detected 25 periodic signals from 23 sources in the LW (Table 2). Our detections fully recover the 10 periodic signals from 10 sources found by Hong et al. (2012). As illustrated in the upper

panel of Figure 6, the measured periods between the two methods agree with each other to within 0.7% and show no systematic bias. The remaining 15 periods are new detections. Since Hong et al. (2012) and this work have used the same set of *Chandra* observations, this difference must be owing to the different period searching methods employed.

Hong et al. (2012) employed the LS periodogram, which, as described in Section 3.1, handles the photometric light curve, while the GL algorithm processes the phase-folded light curve with tolerance for observing gaps. We have applied the LS periodogram to our data in essentially the same way as Hong et al. (2012) and confirmed that only those 10 periods found in their work can be detected by this method. The other 15 periods do not result in a significant detection in the LS periodogram, mainly due to its low efficiency with low-count sources. The detection rate is essentially zero for net counts $\lesssim 100$ and never exceeds 20% for net counts of 150, according to the simulations presented in Hong et al. (2012, figure 7 therein).

For comparison, we provide an estimate on the detection rate of the 10 commonly detected periodic signals using the GL algorithm. For practical purposes we assume an intrinsic sinusoidal shape (Eqn. 2), for which the total counts and period are taken directly from the observed values, whereas the relative amplitude (A_0) is taken from Hong et al. (2012), which was based on the Rayleigh
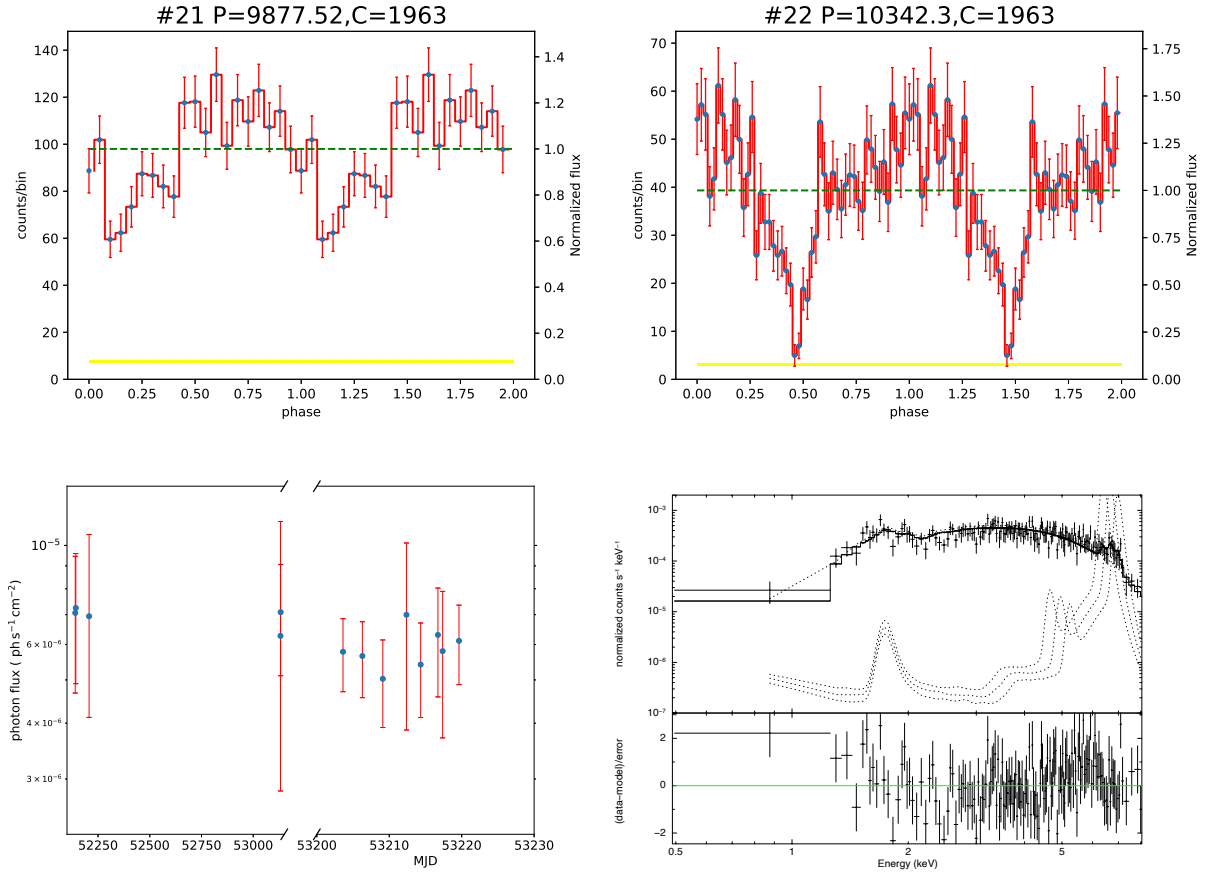
Figure 5. Similar to Figure 4, but for source #21/#22.

statistics (Buccheri et al. 1983; Muno et al. 2003). For each of the 10 signals, 100 simulated light curves are produced and fed to the GL algorithm. Again, we take the 90% probability threshold and a period accuracy of 1% to define a valid detection. The percentage of valid detections, P_{det} (also listed in column 9 of Table 2), is plotted in the upper panel of Figure 6, along with the detection rate of the LS periodogram taken from Hong et al. (2012). Clearly, the GL algorithm works better in almost all cases compared to the LS periodogram.

6.2 Classifying the periodic X-ray sources

While it is generally difficult to unambiguously identify the nature of an X-ray source without knowing its optical counterpart, which is the case for most LW sources, the X-ray temporal and spectral properties of the 23 periodic sources contain important information that actually allow for a reasonable classification for many of them.

First of all, all but one (#25) of these sources are found in the 1–8 keV luminosity range of $10^{31} - 10^{33}$ erg s^{-1}, which is typical of CVs. On the contrary, coronally active binaries (ABs), which are thought to dominate the number of detectable X-ray sources in the LW (Revnivtsev et al. 2009), generally have unabsorbed X-ray luminosities below 10^{31} erg s^{-1} (Sazonov et al. 2006). This stems from the empirical fact that the coronal X-ray emission from low-mass stars saturates at $\sim 10^{-3}$ of the bolometric luminosity (reference). The X-ray spectra of these sources are less informative, since except in one case (#21/#22) they lack the unambiguous sign

of Fe lines due to the moderate S/N (Section 5), which otherwise would be another characteristic signature of CVs (e.g., Xu et al. 2016). Nevertheless, most of these sources do show a very hard continuum that are again typical of CVs, although this could be partly owing to the fact that the parent source list is based on the 2–8 keV band (Section 2.2). Furthermore, the vast majority of the detected periods fall between 1–4 hours, which are also consistent with the known period range of CVs in the solar neighborhood (Ritter & Kolb 2003), as illustrated in Figure 7. Therefore, the global X-ray properties point to CVs dominating the detected periodic sources, a conclusion also drawn by Hong et al. (2012).

The most likely exception is source #25. This source has an unabsorbed 1–8 keV luminosity of 7.5×10^{30} erg s^{-1}, the lowest among all 23 sources. Its X-ray spectra, characterized by a best-fit plasma temperature of 2.3 keV (notably with large uncertainties; Table 3), is also the softest among all sources. These values are more typical of ABs. Moreover, the phase-folded light curve of #25 suggests that the X-ray flux drops to the background level for nearly half of the 47317-sec period (Figure B1). This may be due to either a polar which produces hard X-rays from only one of its two poles, or a total eclipse lasting for half cycle. In the latter case, the eclipsed star cannot be a WD, because of the mismatch between the stellar radius (order 10^4 km) and the orbital separation (order $10^7 e$ km). Rather, the eclipsed star is likely to have a size not much smaller than the orbital separation. The nearly no emission from one star hinted it could be an A-type star which does not produce significant X-rays due to the weakness of surface magnetic field (reference).

Table 3. X-ray spectral properties of the periodic sources

ID (1) LW	$N_{\rm H}$ (2) 10^{22} cm^{-2}	$T_{\rm b}$ (3) keV	$I_{6.4}/I_{6.7}$ (4)	$I_{7.0}/I_{6.7}$ (5)	$I_{6.7}$ (6) 10^{-8} ph cm^{-2} s^{-1}	χ^2/dof (7)	L_{1-8} (8) 10^{31} erg s^{-1}
1†	$0.51^{+0.75}_{-0.34}$	40 (fixed)	-	-	-	1.14/5	$1.82^{+0.64}_{-0.51}$
2	$2.17^{+0.54}_{-0.46}$	$20.7^{+56.9}_{-9.92}$	-	-	-	0.86/78	$23.1^{+2.70}_{-2.01}$
3	$1.34^{+0.70}_{-0.40}$	$46.4^{+46.1}_{-38.5}$	-	-	-	0.98/33	$6.61^{+1.05}_{-0.77}$
4	$1.15^{+0.69}_{-0.50}$	$11.3^{+53.3}_{-4.71}$	-	-	-	0.91/27	$22.5^{+2.94}_{-4.42}$
5	$1.02^{+0.27}_{-0.23}$	40 (fixed)	-	-	-	1.00/33	$5.59^{+0.77}_{-0.70}$
6	$1.82^{+0.57}_{-0.50}$	$6.90^{+12.4}_{-2.90}$	-	-	-	1.12/42	$9.23^{+1.24}_{-1.11}$
7	$1.62^{+0.62}_{-0.49}$	$41.6^{+43.0}_{-32.3}$	-	-	-	0.86/39	$6.70^{+0.89}_{-0.81}$
8	$2.06^{+1.51}_{-0.94}$	40 (fixed)	-	-	-	0.93/7	$1.76^{+0.54}_{-0.42}$
9	$1.29^{+1.34}_{-0.67}$	$20.8^{+95.8}_{-20.8}$	-	-	-	1.10/7	$3.50^{+1.22}_{-0.86}$
10	$2.50^{+7.25}_{-1.56}$	40 (fixed)	-	-	-	0.85/5	$2.14^{+1.76}_{-0.75}$
11	$1.85^{+0.39}_{-0.33}$	40 (fixed)	-	-	-	1.22/47	$9.49^{+1.11}_{-1.02}$
12	$6.23^{+9.67}_{-3.66}$	40 (fixed)	-	-	-	0.78/6	$7.58^{+5.76}_{-2.93}$
13	$0.90^{+0.30}_{-0.24}$	40 (fixed)	-	-	-	1.15/38	$8.48^{+1.12}_{-1.04}$
14†	$0.51^{+0.75}_{-0.34}$	40 (fixed)	-	-	-	1.14/5	$1.82^{+0.64}_{-0.51}$
15	$1.46^{+0.48}_{-0.38}$	40 (fixed)	-	-	-	1.16/42	$12.8^{+1.77}_{-1.61}$
16	$0.89^{+0.18}_{-0.16}$	40 (fixed)	-	-	-	1.43/51	$8.47^{+0.88}_{-0.83}$
17	$2.68^{+0.63}_{-0.52}$	40 (fixed)	-	-	-	0.75/36	$11.3^{+1.61}_{-1.45}$
18	$2.01^{+0.92}_{-0.66}$	40 (fixed)	-	-	-	0.53/14	$4.21^{+0.89}_{-0.77}$
19	$1.82^{+0.10}_{-0.10}$	40 (fixed)	-	-	-	0.95/185	$83.9^{+3.25}_{-3.16}$
20	$2.09^{+2.45}_{-1.16}$	$4.04^{+28.2}_{-2.54}$	-	-	-	1.04/12	$5.39^{+1.81}_{-1.47}$
21‡	$2.83^{+0.25}_{-0.23}$	40 (fixed)	$0.47^{+0.72}_{-0.35}$	$0.91^{+1.22}_{-0.56}$	31.7	1.10/147	$60.00^{+3.25}_{-3.12}$
22‡	$2.83^{+0.25}_{-0.23}$	40 (fixed)	$0.47^{+0.72}_{-0.35}$	$0.91^{+1.22}_{-0.56}$	31.7	1.10/147	$60.00^{+3.25}_{-3.12}$
23	$1.83^{+0.44}_{-0.37}$	40 (fixed)	-	-	-	1.47/35	$9.23^{+1.22}_{-1.13}$
24	$0.35^{+0.16}_{-0.13}$	$4.78^{+3.55}_{-1.58}$	-	-	-	1.19/55	$8.73^{+1.09}_{-0.98}$
25	$0.83^{+3.31}_{-0.83}$	$2.30^{+1.59}_{-0.85}$	-	-	-	0.80/2	$0.75^{+0.30}_{-0.28}$
H	$1.99^{+0.10}_{-0.97}$	40 (fixed)	$0.28^{+0.10}_{-0.09}$	$0.78^{+0.18}_{-0.16}$	$8.76^{+3.57}_{-3.57}$	1.19/205	$31.8^{+0.95}_{-0.95}$
L	$1.33^{+0.12}_{-0.11}$	40 (fixed)	< 0.18	< 0.39	$2.53^{+1.10}_{-1.10}$	1.09/168	$5.36^{+0.24}_{-0.24}$

Notes: (1) Source sequence number as in Table 2, except "H" and "L", which refer to the bright and faint group of sources, i.e., having 1–8 keV luminosity above (below) 10^{32} erg s^{-1}. †Sources 1 and 14 are the same source with two different periods; ‡Sources 21 and 22 are the same source with two different periods. (2) Line-of-sight absorption column density. (3) The bremsstrahlung temperature, in units of keV. Fixed at a value of 40 keV when the spectrum provides no signficant constraint to this parameter. (4)-(5) Flux ratio of the 6.4 or 7.0 keV line to the 6.7 keV line. (6) Integrated flux of the 6.7 keV line. (7) χ^2 and degree of freedom of the best-fit model. (8) 1–8 keV unabsorbed luminosity. Quoted errors are at the 90% confidence level.

Then the orbit radius would be around 0.02 AU, taking $3M_\odot$ as the total mass.

For non-magnetic CVs like DNe, the common phase-folded light curve exhibits narrow dip, due to the eclipse of the white dwarf, as modeled in Section 3.3. The typical light curve is like #22 in Figure 5. While the simultaneous existence of #21 and #22 and the 2% period difference suggest it might be an asynchronous intermediate polar. Besides, the central dip of #3, #18 and #20 are also similar to this circumstance. Since the eclipse happens in nearly all types of CVs, we could only set three as an upper limit of number of DNe in our sample.

For magnetic CVs, including IPs and polars, their orbit modulation could give rise to more complicated shape of light curve. For polars, consider the simplistic situation, whose accretion is nearly onto one pole, then the shape of light curve would be divided into two groups. Suppose an inclination i, the angle between rotation axis and magnetic axis is β, the magnetic colatitude of accretion is ϵ. Then if $i + \beta + \epsilon > 90°$, we would see alternately two poles, the shape would be like #6, with half of orbit cycle showing no emission. This so-called "two-pole" behavior are more complicated if the accretion goes to both two poles, the gap with half orbit cycle would be partially filled (like #16) by second pole's emission or even making the light curve constant. Sometimes it may completely reverse in hard X-ray band cause the accretion shock in second pole producing most of hard X-rays (Heise et al. 1985). On the other hand, if $i + \beta + \epsilon < 90°$ and $\beta < i$, the accreting pole would be always visible. In that case, the X-ray flux would be roughly constant, although sometimes some dips may been seen due to the obscuring of accretion stream.

For IPs, the orbital modulation could be resulted by eclipse of WD, the absorption of X-rays emitted near the white dwarf surface (Hellier et al. 1993), or the "disc-overflow" model in (Norton et al.
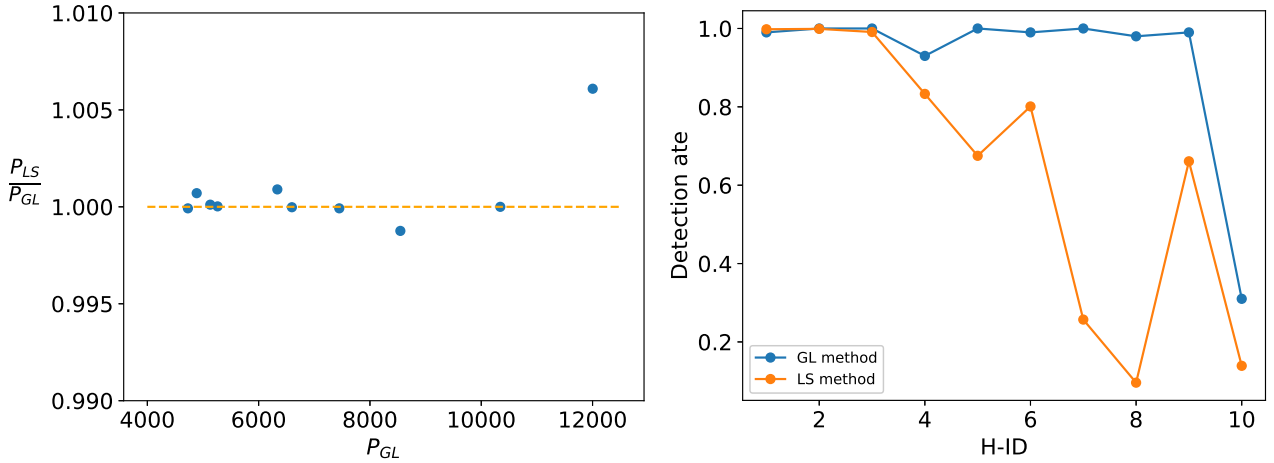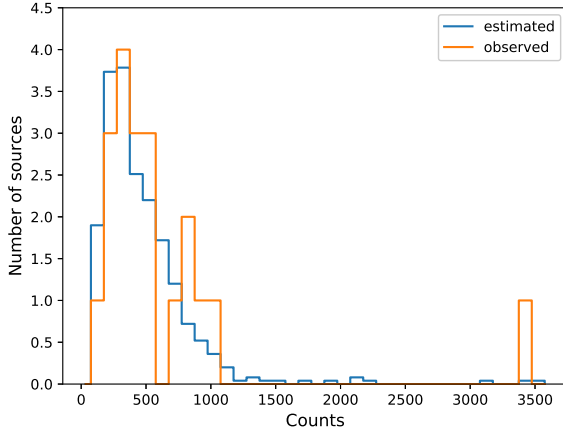
Figure 6. Comparison between the periods (*left*) and detection rate (*right*) of the 10 signals commonly found by the GL and LS methods.The H-ID is the sequence number given in Hong et al. (2012), same as listed in column 6 of Table 2.
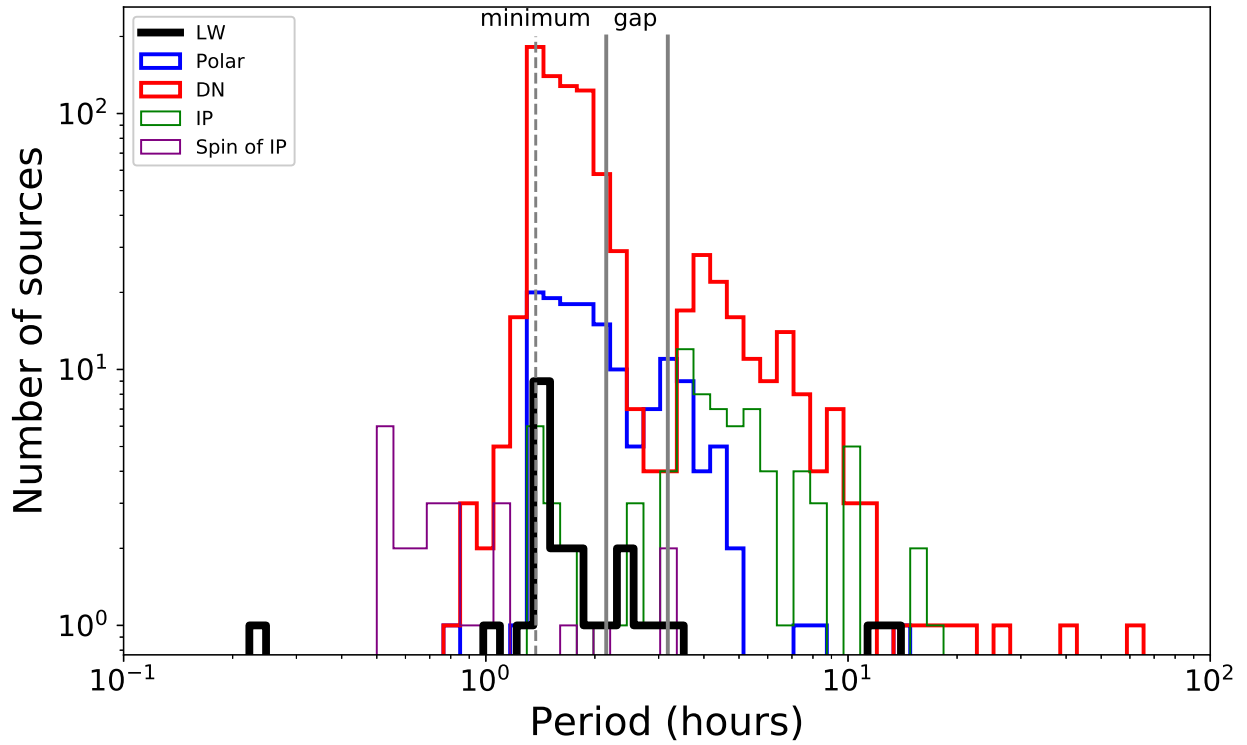
Figure 7. The period distribution of the LW sources (dark-blue line), the spin (purple) and orbital (green) periods of IPs ,the periods (sky-blue) of polars and the orbital (red) periods of DNe from the RK catalog (Ritter & Kolb 2003), version 7.20). The famous period gap(yellow line) and period minimum(orange dashed line) are also plotted, whose value are taken from (Knigge et al. 2011).

1996). The shape of light curve in IPs could be any kinds of dips or sinusoidal variation. The only robust identification is to determine both their spin and orbital period, like the #1(#14) and #21(#22) in our sample. Two of these periodic sources, #1(14) and #21(22) can be determined as they have two confirmed period. For source #1, the width in phase with flux lower than average is about 0.5, longer than the value for #14, which is about 0.3. This difference holds out the view that the short period caused by rotation with the alternation of accretion column. While for source #21, the weak variation indicates the rotation modulation. And the apparent sharp, narrow eclipsing in #22 strongly sustain that the orbit modulation with high inclination angle. Considering that the angle between magnetic axis and rotation axis is usually small, it also support for the weak variation of spin modulation. Before we start to discuss the

Figure 8. The comparison between estimated and the real detected number of sources.

Figure 9. Probability of eclipsing in CVs. The break around 3.2hours resulted by different model for CVs beyond and below the period gap.

nature of other periodic sources, we should take a look at CVs in the field. Their period distribution, including polars, IPs and DNe, are shown in Figure 7. It can be easily seen that the period distribution of these LW sources resembles those of polars more than others, since most of these are below the period gap. While DNe and IPs both have a considerable number of systems with period beyond the gap. According to the our simulation results in Section 3.3, this can not be resulted from selection bias of algorithm.

Based on our current understanding of the shape and distribution of orbital modulation, we conclude that the periodic sources discovered are mostly polars, with several IPs(two determined) and DNe(three as upper limit).

6.3   CV populations in the Galactic bulge

Firstly, we assumed that the fraction of polars in the total sample of 667 sources is α and the sinusoidal variation happens only in "two-pole" situation, which takes $90°$ in total $180°$. In most case, the accretion of polar falls onto one pole. Then we can set 25% ($50\% \times 50\%$) as the lower limit of fraction for polars with sinusoidal variation intrinsically. We assumed the even distribution for amplitude from 0.5 to 0.9 and took the simulation results for P=5540s and P=45540s as the detection rate for period under(60% of the total number) and beyond the period gap(40% of the total number). The value of 60% and 40% are estimated from Figure 7. Then we set width=100 for our binning of counts, from 75 to 3575, covering nearly all detected sources. The predicted number of periodic sources which "should" be detected in each bin is calculated by:

$$Np_i = N_i \times DR \times 25\% \times 667 \times \alpha \qquad (4)$$

N_i is the product of number of sources detected in the bin. DR denotes the detection rate weighted from simulation. Then we sum all Np_i together and force it equals to 20, getting α about 16%. The comparison between Np_i and the real detected 20 periodic sources(two determined IPs and one AB excluded) are plotted in Figure 8. The perfect agreement between their population proves the validity of estimation.

Since the real luminosity function should be gentle than that of total sample, which means there could be more polars at the bright band, then it demanding lower numbers of polar to balance the high
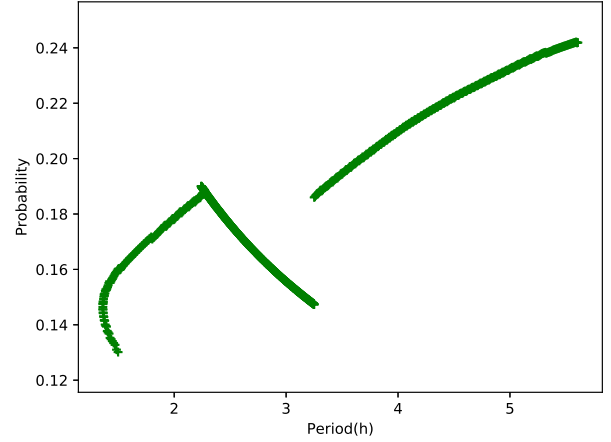
detection rate for bright sources. Besides, with the intrinsic fraction (25% as the lower limit) increasing, the α decreasing. In general, the 16% should be treated as the upper limit for polars, especially when we considered all the 20 sources(already excluding the two IPs) are polars.

While for DNe, we are constrained by lack of reliable X-ray luminosity function(XLF). We have already set the three as the upper limit of DNe in Section 6.2. However, the steeper XLF for DNe than the XLF for total sample would only contribute the lower limit for their proportion. Though this conflict leads to the uncertainty of estimation, we still present the estimation for fraction of DNe as supplement. Intrinsically, the eclipse of white dwarf depends on the inclination angle, radius of companion star and orbit. If we set i as inclination, R_1, R_2, R_{orb} as radius of WD, companion star and orbit respectively. then eclipsing happens when :

$$R_{orb} \times cos(90 - i) \leq R_1 + R_2 \qquad (5)$$

Assuming that inclination angle is even distributed in $(0, 90°)$, the probability of eclipsing(hereafter EP) are plotted in Figure 9. The value of R_1, R_2 and R_{orb} are taken from simulation operated by (Knigge et al. 2011), in which R_1 is fixed at when M_{WD} equals 0.75 solar mass.

We utilized the simulation results of 5258s and 15258s as the detection rate for period under (75% of the total number) and beyond (25% of the total number) the period gap. The fraction is also taken from the statistics as shown in from Figure 7. Besides, EP was chosen as 0.18 and 0.20 for this two types. Similarly, the predicted number of periodic non-mCVs which "should" be detected in each counts bin is:

$$Np_i = N_i \times DR \times EP \times 667 \times \alpha \qquad (6)$$

Since the sum of Np_i was assigned as three, the α would be around 0.45 if we set 10^{32} erg s^{-1} (roughly corresponding 675 counts) as the upper limit of luminosity for DNe. The rationality of the limit has been proved by the DNe sample from solar neighborhood in (Xu et al. 2016), based on *Suzaku* observation. The uncertainty of this fraction comes from our limited acquaintance about XLF for DNe, and the subjective diagnostic for the phase-folded light curve.

7 SUMMARY

1. We have discovered 23 periodic sources with 25 signal in the LW by using GL method, including 10 of them already found by LS method in Hong et al. (2012). Their luminosity range locates at $10^{31} - 10^{33}$ erg s^{-1}. The general feature of these 23 sources resembles that of polars. Three of them with narrow dip are likely DNe. Two of them are determined as IP.

2. We estimate the mass of WD from a source with great identification for Fe XXVI and Fe XXV emission lines, i.e. 0.8 $M_\odot$ for #21(#22) as being an IP.

3. We provide well-constrained fraction of polars in the whole sample, i.e, 16% as the upper limit. The estimation on fraction of non-mCVs is about 45% while the certainty is restricted by limited appreciation about their XLF. Combined with the period distribution, we conclude that the periodic sources are mainly polars with relatively harder spectra, especially in the luminosity range that lower than 10^{32} erg s^{-1}. Besides, the H sources ($L>10^{32}$ erg s^{-1}), whose emission is mostly contributed by IPs, indicate $M_{WD} \sim 0.8 M_\odot$, consistent with the previous result $0.8 \pm 0.07 M_\odot$ in (Yu et al. 2018).

4. The lower luminosity and narrow eclipsing model for orbital modulation reduced the detection rate simultaneously for periodicity. That may explain why we had no trace on non-mCVs in GCR in earlier period searching work.

5. We proved the higher detection rate, more usage of data and ignorance of observation gap for GL method compared with LS method. It is noteworthy that the shape of light curve in GL method could be modified according to different scenarios. It was applied on detection of planetary transits by using customized eclipsing model (Aigrain & Favata 2002). For the utility of GL method, there is still room for improvement in the future.

REFERENCES

Aigrain S., Favata F., 2002, A&A, 395, 625
Buccheri R., et al., 1983, A&A, 128, 245
Cheng Z., Li Z., Li X., Xu X., Fang T., 2019, ApJ, 876, 59
Cicuttin A., Colavita A. A., Cerdeira A., Mutihac R., Turrini S., 1998, ApJ, 498, 666
Deeming T. J., 1975, Ap&SS, 36, 137
Edelson R. A., Krolik J. H., 1988, ApJ, 333, 646
Gregory P. C., Loredo T. J., 1992, ApJ, 398, 146
Hailey C. J., et al., 2016, ApJ, 826, 160
Heise J., Brinkman A. C., Gronenschild E., Watson M., King A. R., Stella L., Kieboom K., 1985, A&A, 148, L14
Hellier C., Garlick M. A., Mason K. O., 1993, MNRAS, 260, 299
Hong J., 2012, MNRAS, 427, 1633
Hong J. S., van den Berg M., Grindlay J. E., Laycock S., 2009, ApJ, 706, 223
Hong J., van den Berg M., Grindlay J. E., Servillat M., Zhao P., 2012, ApJ, 746, 165
Knigge C., Baraffe I., Patterson J., 2011, ApJS, 194, 28
Leahy D. A., Darbro W., Elsner R. F., Weisskopf M. C., Sutherland P. G., Kahn S., Grindlay J. E., 1983, ApJ, 266, 160
Lomb N. R., 1976, Ap&SS, 39, 447
Morihana K., Tsujimoto M., Yoshida T., Ebisawa K., 2013, ApJ, 766, 14
Muno M. P., Baganoff F. K., Bautz M. W., Brand t W. N., Garmire G. P., Ricker G. R., 2003, ApJ, 599, 465

Muno M. P., et al., 2009, ApJS, 181, 110
Norton A. J., Beardmore A. P., Taylor P., 1996, MNRAS, 280, 937
Revnivtsev M., Sazonov S., Churazov E., Forman W., Vikhlinin A., Sunyaev R., 2009, Nature, 458, 1142
Revnivtsev M., Sazonov S., Forman W., Churazov E., Sunyaev R., 2011, MNRAS, 414, 495
Ritter H., Kolb U., 2003, A&A, 404, 301
Sazonov S., Revnivtsev M., Gilfanov M., Churazov E., Sunyaev R., 2006, A&A, 450, 117
Scargle J. D., 1982, ApJ, 263, 835
Schuster A., 1898, Terrestrial Magnetism (Journal of Geophysical Research), 3, 13
Schwarzenberg-Czerny A., 1996, ApJ, 460, L107
Silber A. D., 1992, PhD thesis, MASSACHUSETTS INSTITUTE OF TECHNOLOGY.
Stellingwerf R. F., 1978, ApJ, 224, 953
Wevers T., et al., 2016, MNRAS, 462, L106
Xu X.-J., Wang Q. D., Li X.-D., 2016, ApJ, 818, 136
Xu X.-J., Li Z., Zhu Z., Cheng Z., Li X.-d., Yu Z.-l., 2019, ApJ, 882, 164
Yu Z.-l., Xu X.-j., Li X.-D., Bao T., Li Y.-x., Xing Y.-c., Shen Y.-f., 2018, ApJ, 853, 182
Zhu Z., Li Z., Morris M. R., 2018, ApJS, 235, 26
van den Berg M., Hong J. S., Grindlay J. E., 2009, ApJ, 700, 1702

APPENDIX A: A BRIEF INTRODUCTION TO THE GREGORY-LOREDO ALGORITHM

The basic rules for Bayesian probabilities are the sum rule:

$$p(H_i|I) + p(\bar{H}_i|I) = 1 \qquad (A1)$$

And the product rule:

$$p(H_i, D|I) = p(H_i|I) \cdot p(D|H_i, I) = p(D|I) \cdot p(H_i|D, I) \qquad (A2)$$

From equation A2 we could easily derive Bayes's theorem.

$$p(H_i|D, I) = p(H_i|I) \cdot \frac{p(D|H_i, I)}{p(D|I)} \qquad (A3)$$

The symbols in this work follow the same expression used in (Gregory & Loredo 1992). Throughout this work, these symbols could be briefly practically understood. H_i signifies model, D signifies dataset, I represents the ensemble of all the hypotheses considered i.e. all the model used. GL method employs piecewise function for periodic signal. Each model has $(m + 2)$ parameters: angular frequency $\omega = 2\pi/P$, P represents period; phase parameter ϕ; and m values r_j, signifies the counts rate in each phase bin where j=1 to m. The following we replace H_i with M_i to denote the model where i represents the number of bins in piecewise model. Then the Bayes's theorem can be written as:

$$p(M_i|D, I) = p(M_i|I) \cdot \frac{p(D|M_i, I)}{p(D|I)} \qquad (A4)$$

We could write $I = M_1 + M_2 + M_3 + \cdots$, where "+" stands for "or". Thus the proposition (M_i,I) is true if and only if model M_i is true i.e. (M_i,I) = M_i. GL method defines odds ratio to make the model comparison.

$$O_{ij} = \frac{p(M_i|D, I)}{p(M_j|D, I)} = \frac{p(M_i|I)}{p(M_j|I)} \cdot \frac{p(D|M_i)}{p(D|M_j)} \qquad (A5)$$

Note that M_1 means constant model, M_i(i=2,3,4 $\cdots N_{mod}$, where N_{mod} is the total number of models considered.) represents periodic model. The probabilities for each model can be deduced by A5

$$p(M_i|D, I) = O_{i1} \cdot p(M_1|D, I) \qquad (A6)$$

$$p(M_1|D,I) = \frac{\sum_{j=1}^{N_{mod}} p(M_j|D,I)}{\sum_{j=1}^{N_{mod}} O_{j1}} = \frac{1}{\sum_{j=1}^{N_{mod}} O_{j1}} \tag{A7}$$

Substitute A7 into A6, we got

$$p(M_i|D,I) = \frac{O_{i1}}{\sum_{j=1}^{N_{mod}} O_{j1}} \tag{A8}$$

Then the probability that the signal is periodic is :

$$p(M_m(m > 1)|D,I) = \frac{\sum_{m=2}^{m_{max}} O_{m1}}{1 + \sum_{m=2}^{m_{max}} O_{m1}} \tag{A9}$$

The odds ratio can be calculated by the probability for model:

$$O_{m1} = \frac{p(M_m|D.I)}{p(M_1|D.I)} \tag{A10}$$

Using Bayes's theorem shown as A4,

$$O_{m1} = \frac{p(M_m|I) \cdot p(D|M_m)}{p(M_1|I) \cdot p(D|M_1)} \tag{A11}$$

Following the same assignment by (Gregory & Loredo 1992), we also consider the probability of periodic and aperiodic signals are the same. Then the priors for model can be written explicitly as :

$$p(M_1|I) = \frac{1}{2} \tag{A12}$$

$$p(M_m|I) = \frac{1}{2\nu}, \quad \nu = m_{max} - 1 \tag{A13}$$

Since the essence of the algorithm is not our subject, we directly introduce the Eqn. 5.27 in (Gregory & Loredo 1992) as follows. It must be emphasized that this equation worked for the situation when the period and phase are both unknown.

$$p(D|M_m) = \frac{\Delta t^N (m-1)! N! \gamma(N+1, A_{max}) T}{2\pi A_{max}(N+m-1)! T^{N+1} \ln(\omega_{hi}/\omega_{lo})}$$
$$\times \int_{w_{lo}}^{w_{hi}} \frac{d\omega}{\omega} \times \int_0^{2\pi} d\phi \frac{m^N}{W_m(\omega,\phi)} \tag{A14}$$

Substituting $m = 1$ into A14, we got:

$$p(D|M_1) = \frac{\Delta t^N N! \gamma(N+1, A_{max}) T}{A_{max} N! T^{N+1}} \tag{A15}$$

Substituting A12, A13, A14, A15 into A11, the odds ratio could be written as follows, which is the same as equation 5.28 in GL method:

$$O_{m1} = \frac{1}{2\pi\nu \ln(\omega_{hi}/\omega_{lo})} \binom{N+m-1}{N}^{-1} \times \int_{w_{lo}}^{w_{hi}} \frac{d\omega}{\omega}$$
$$\times \int_0^{2\pi} d\phi \frac{m^N}{W_m(\omega,\phi)} \tag{A16}$$

In astronomical dataset, the observation always brings data gaps. For example, when the period is long and the exposure time for single observation is low, different bins may not be covered fairly. Then the initial assumptions above mentioned may fail, leading to some fake detections especially at low frequencies. In appendix B to (Gregory & Loredo 1992), a solution to this problem has been proposed. They defined a weighting factor $S(\omega,\phi)$, where $\tau_j(\omega,\phi)$

signifies the exposure time in each bin:

$$S(\omega,\phi) = \prod_{j=1}^m s_j^{-n_j} \tag{A17}$$

$$s_j(\omega,\phi) = \frac{\tau_j(\omega,\phi)}{T/m} \tag{A18}$$

Then the odds ratio should be modified as:

$$O_{m1} = \frac{1}{2\pi\nu \ln(\omega_{hi}/\omega_{lo})} \binom{N+m-1}{N}^{-1} \times \int_{w_{lo}}^{w_{hi}} \frac{d\omega}{\omega}$$
$$\times \int_0^{2\pi} d\phi \frac{S(\omega,\phi)m^N}{W_m(\omega,\phi)} \tag{A19}$$

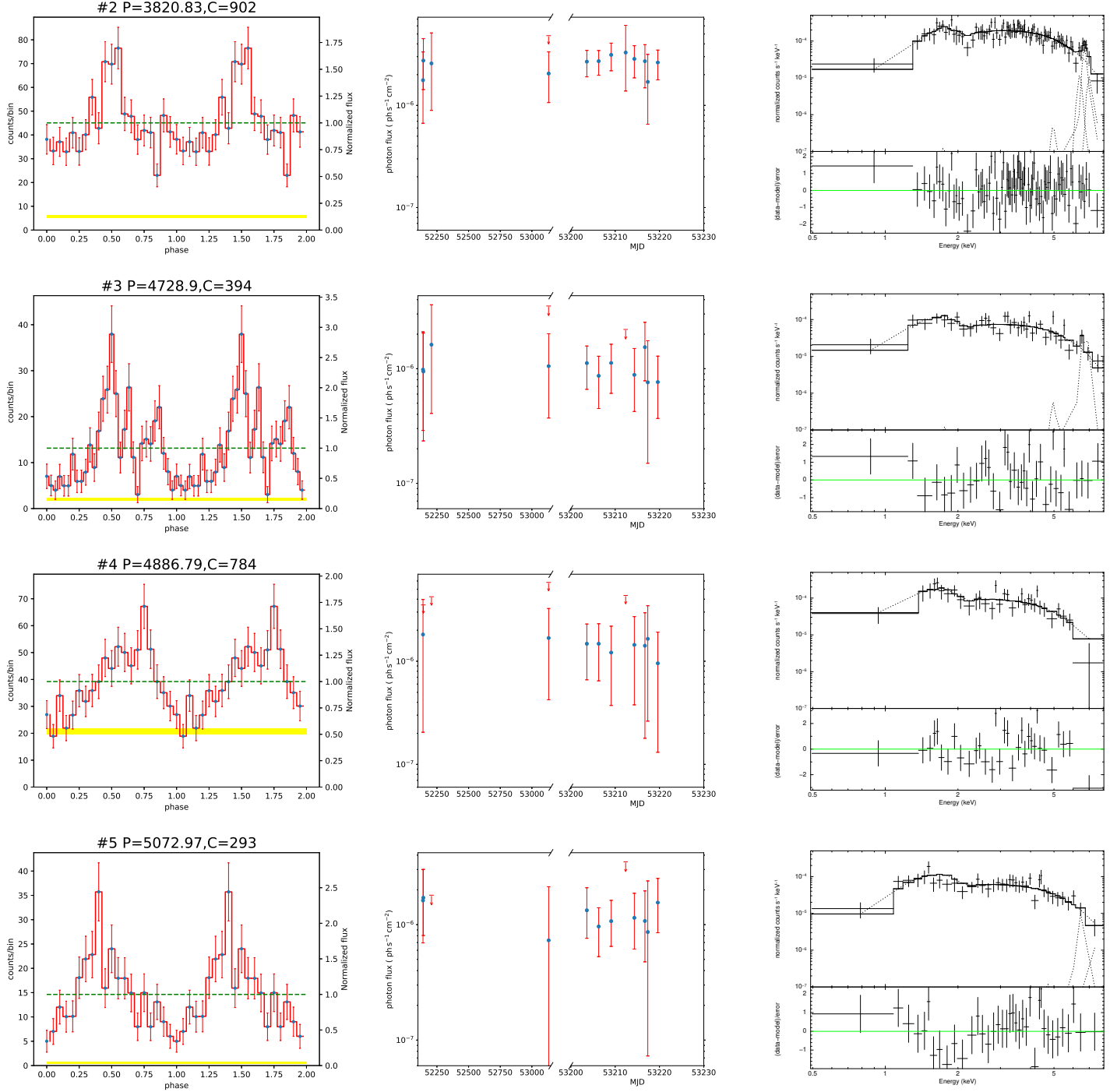Ultimately, the probability of whether the dataset is periodic is:

$$p(periodic) = \frac{\sum_{m=2}^{m_{max}} O_{m1}}{1 + \sum_{m=2}^{m_{max}} O_{m1}} \tag{A20}$$

The posterior probability of the frequency indicates the period of the signal:

$$O_{m1}(\omega) = \frac{1}{2\pi\nu} \binom{N+m-1}{N}^{-1} \times \int_0^{2\pi} d\phi \frac{S(\omega,\phi)m^N}{W_m(\omega,\phi)} \tag{A21}$$

The period locates at $P = 2\pi/\omega$ when $O_{m1}(\omega)$ takes the highest value.

APPENDIX B: ADDITIONAL FIGURES OF THE PERIODIC X-RAY SOURCES

Figure B1. The phase-folded light curve (left) , the long-term, inter-observation light curve (middle) and the spectra (right) for all the source in Table 2, similar to Figure 4.
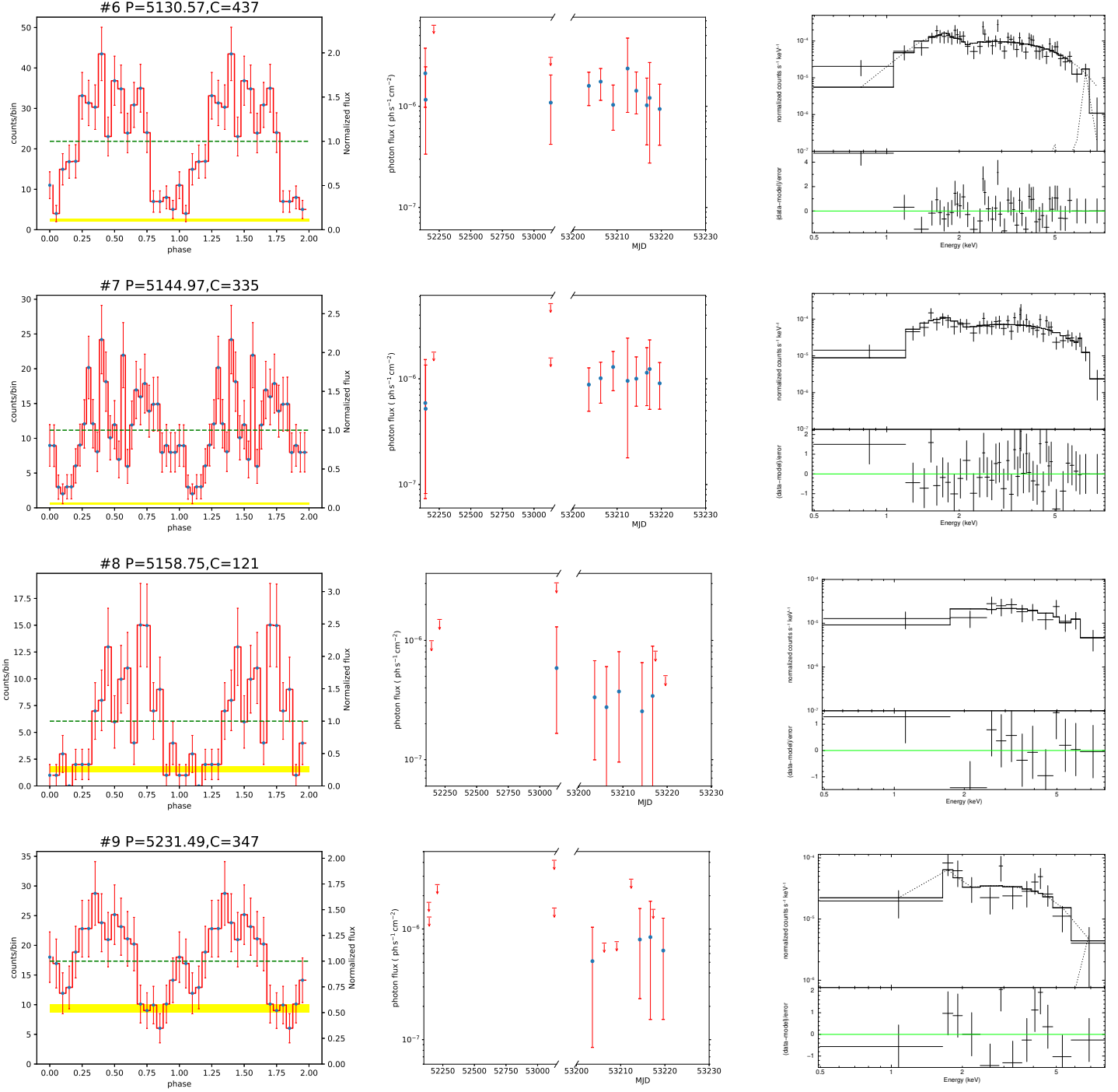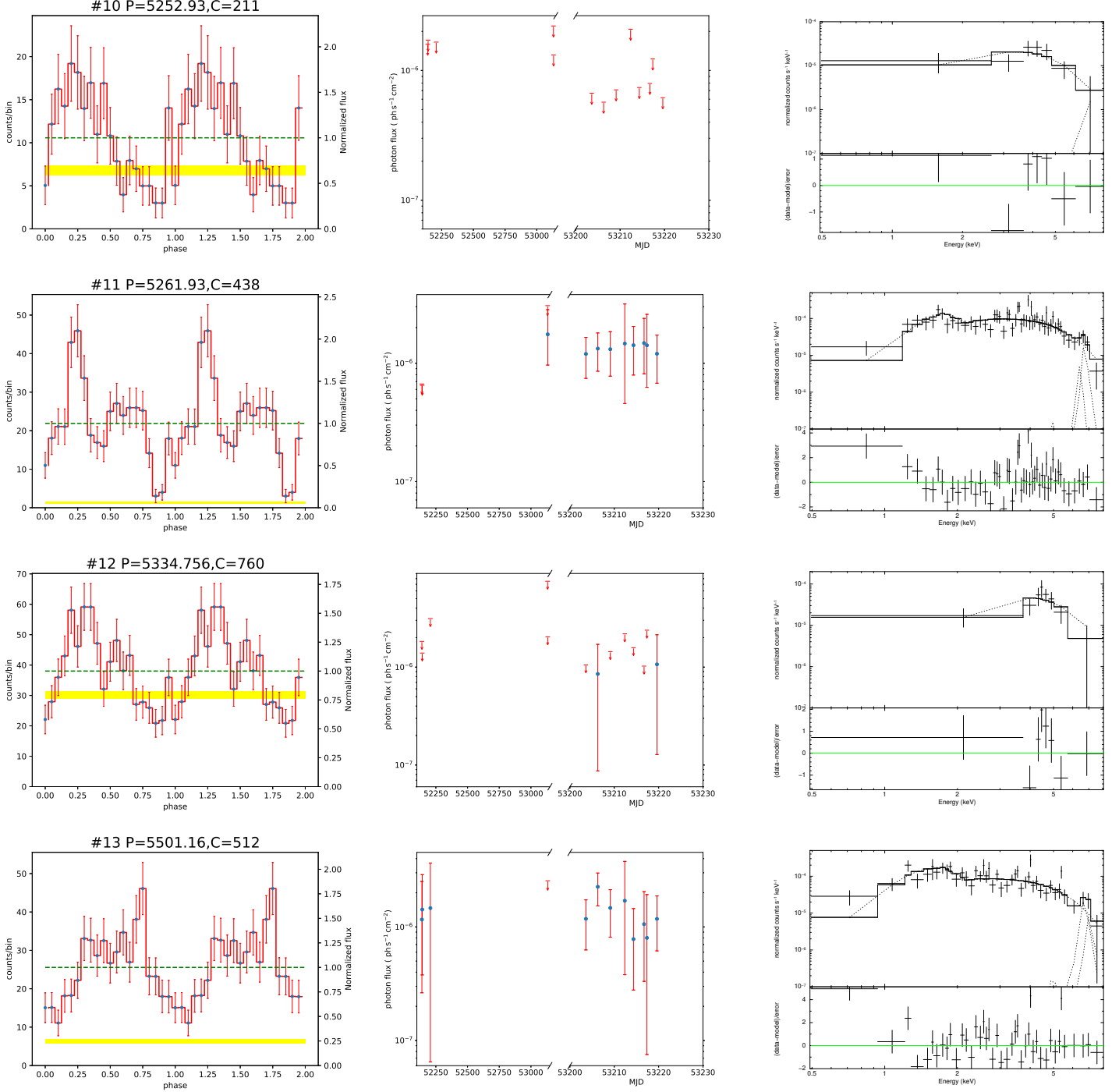
Figure B2. First figure continued
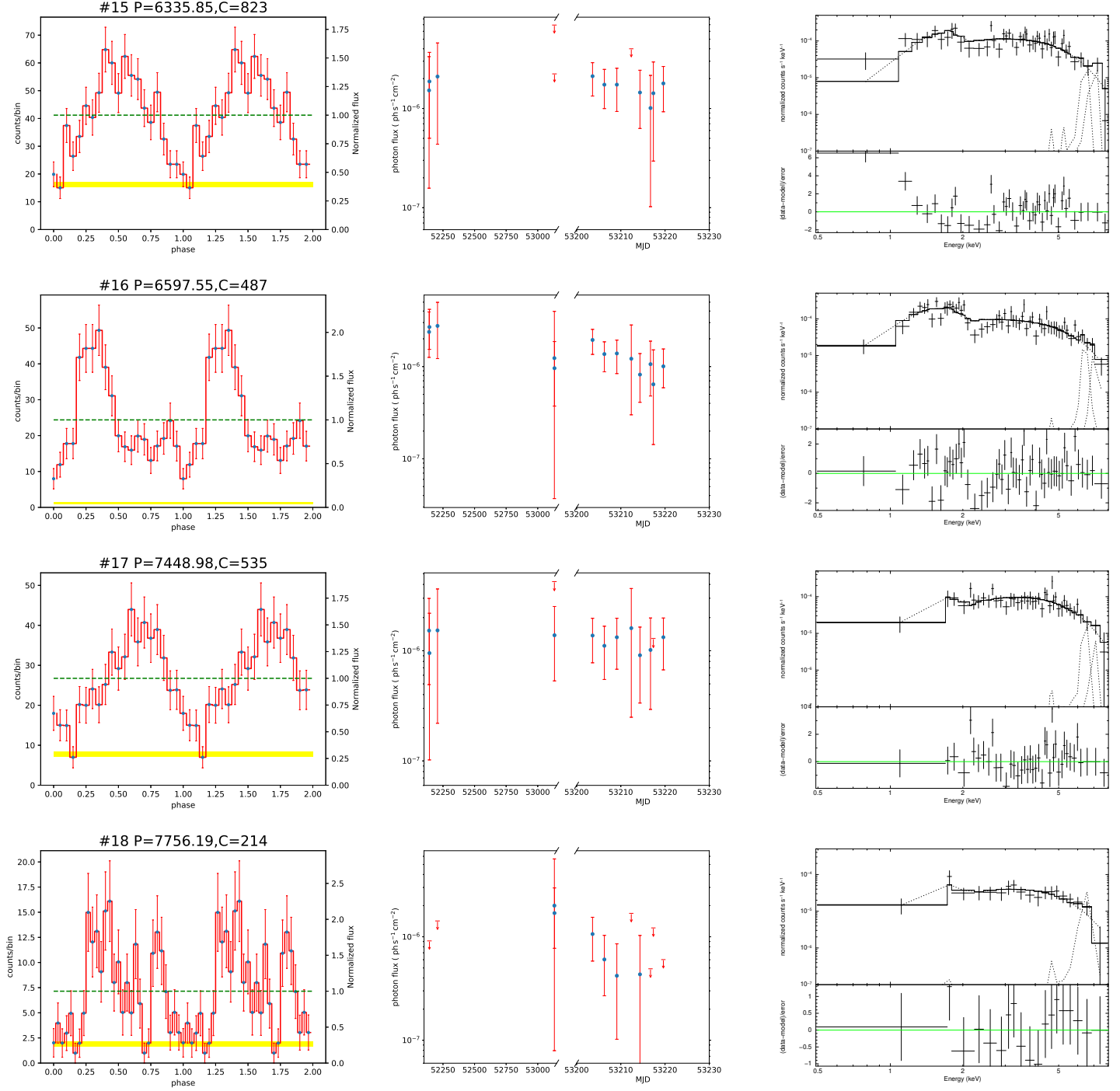
Figure B3. First figure continued
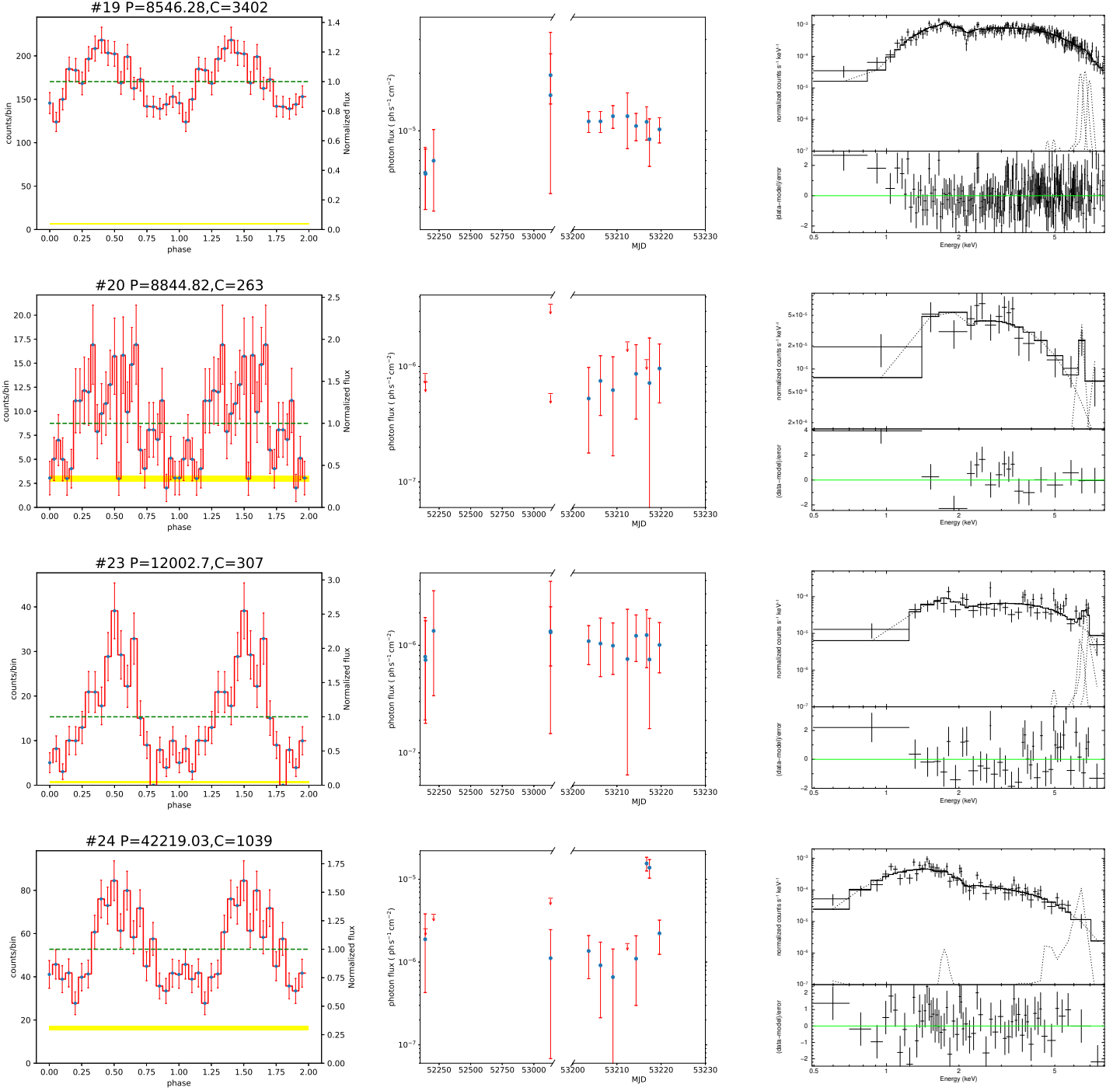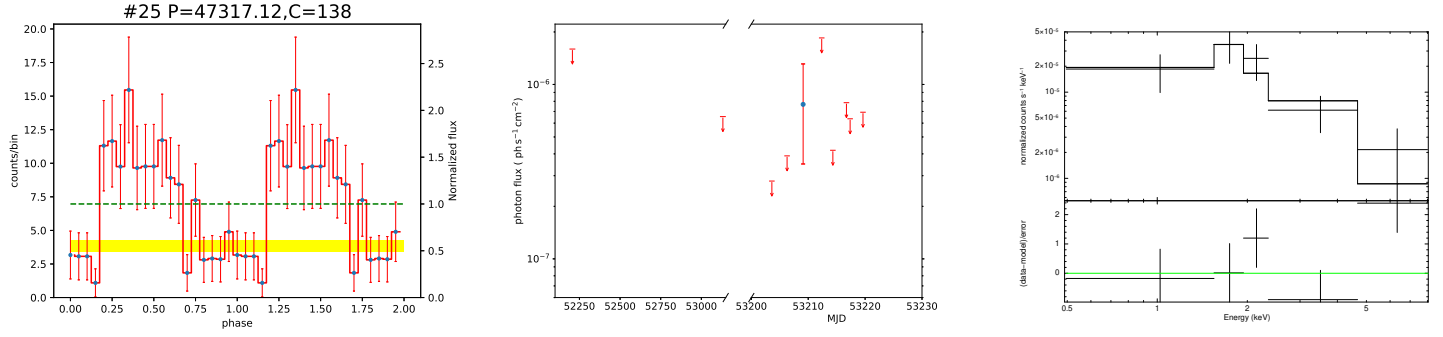
Figure B4. First figure continued

Figure B5. First figure continued

Figure B6. First figure continued